Microwave Imaging Reflectometry Experiment in TPE-RX

Yoshio NAGAYAMA, Soichiro YAMAGUCHI[1], Zhongbing SHI[2], Yuichiro KOGI[3],
Atsushi MASE[3], Shoji SUGITO, Yoichi HIRANO[4], Satoru KIYAMA[4], Haruhisa KOGUCHI[4],
Hajime SAKAKITA[4], Kiyoyuki YAMBE[4] and Nobuyoshi OHYABU

National Institute for Fusion Science, Toki 509-5292, Japan
[1]*Kansai University, Suita 564-8680, Japan*
[2]*The Graduate University for Advanced Studies, Toki 509-5292, Japan*
[3]*KASTEC, Kyushu University, Kasuga 816-8580, Japan*
[4]*National Institute of Advanced Industrial Science and Technology, Tsukuba 305-8568, Japan*

Microwave imaging reflectometry (MIR) was developed in TPE-RX, one of the world's largest reversed field pinch (RFP) devices. The system optics are made of aluminum mirrors, Teflon lenses, and Plexiglas plates in order to reduce size. In this system, frequencies are stabilized so that noise can be reduced using narrow bandpass filters. A 4×4 2-D mixer array and phase detection system have also been developed. With this system, density fluctuations in the high-Θ RFP plasma, pulsed poloidal current drive (PPCD) plasma, and quasi-single helicity (QSH) plasma are observed in TPE-RX. This is the first MIR experiment in an RFP device.

1. Introduction

Microwave reflectometry is a powerful tool to study turbulence and instabilities in plasmas because it provides sensitive measurement of density fluctuations, by monitoring reflection of microwaves by the plasma at the cutoff density [1]; density fluctuations cause amplitude and phase modulation in the reflected beam. Recently microwave imaging reflectometry (MIR) has been intensively developed [2]. MIR takes advantage of large-aperture optics to form an image of the reflecting layer onto an array of detectors located at the image plane, enabling localized sampling of small plasma areas.

A reversed field pinch (RFP) plasma is sustained by the dynamo effect, a mechanism by which the toroidal plasma current causes a toroidal magnetic field. The dynamo effect is a famous example of the self-organization, a major topic in the physics of complexity. The dynamo effect is believed to be caused by turbulence and instabilities, but microwave reflectometry has not been applied to RFP plasma. One reason may be the limitations of the viewing port. Actually, the diameter of the TPE-RX viewing port is 10 cm, similar to the open mouth (10.5 × 8.7 cm) of the 20 dB standard gain horn antenna for 20 GHz (WR-42). MIR can be applied to RFP, as the microwave beam can be optically adjusted to the window. This paper will present an MIR experiment in TPE-RX, an RFP device at the National Institute of Advanced Industrial Science and Technology (AIST) [3]. This experiment is the first MIR experiment in an RFP device.

author's e-mail: nagayama.yoshio@nifs.ac.jp

MIR is under development at the National Institute for Fusion Science (NIFS) in collaboration with Kyushu University [4]. MIR can be improved by: improving sensitivity or the signal-to-noise ratio, improving the number of channels in the 2-D detector array, and reducing the cost. The first MIR system has been installed in Large Helical Device [4, 5]. In this system, microwaves are generated by impact ionization avalanche transit-time (IMPATT) oscillators, because of their high output power. Since microwaves generated by IMPATT oscillators have many modes with slightly different frequencies, phase detection is impossible. The MIR system installed in TPE-RX is relatively advanced featuring: (1) narrow intermediate frequency (IF) bandwidth, (2) a 2-D receiver array, and (3) phase detection.

2. The MIR System in TPE-RX

TPE-RX is one of the largest RFP devices in the world; with a major radius of 172 cm and a minor radius of 45 cm. Figure 1 (a) shows the line-averaged electron density of the typical pulsed poloidal current drive (PPCD) RFP plasma. From the line-averaged electron density, which is measured by two-color CO_2 laser interferometers in two chords, the electron density profile is obtained under the assumption

$$n_e(x) = n_{e0}(1 - x^4)(1 + Bx^2), \qquad (1)$$

where $x = r/a$ and a is the minor radius of the plasma. Parameters n_{e0} and B are determined by fitting the data to Eq. (1). Figure 1 (c) shows the obtained electron density
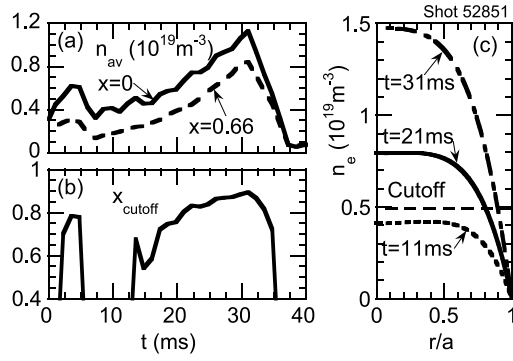
Fig. 1　(a) Line-averaged electron density (n_{av}) measured using the CO_2 laser interferometers, (b) the radius of the cutoff layer (r_c), and (c) the electron density profiles in a typical pulsed poloidal current drive (PPCD) plasma in TPE-RX.
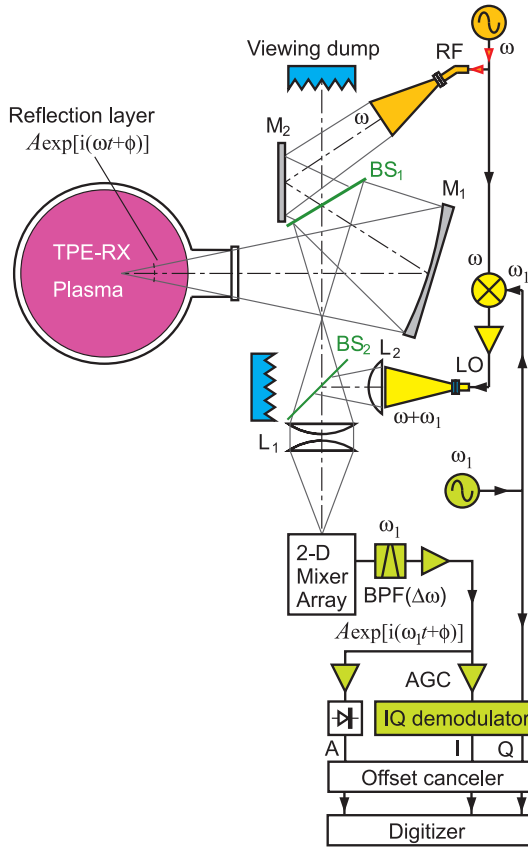

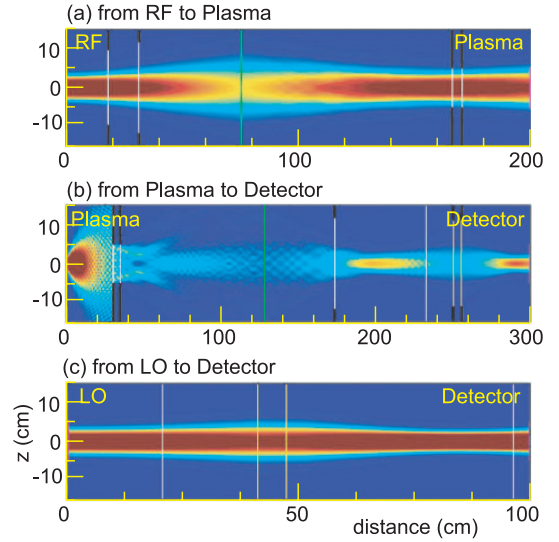Fig. 2　Schematic view of MIR system in TPE-RX.

Fig. 3　The finite difference time domain method (FDTD) simulation of microwave propagation in the TPE-RX plasma. Contour plots is proportional to microwave power ($|E|^2$). (a) Illumination microwave beam from the horn antenna of the RF source to the plasma. (b) Scattered wave at a single point in the plasma to the detector. (c) LO wave traveling to the detector. Vertical green lines indicate concave mirrors, yellow lines Teflon lenses, blue lines beam splitters, and black lines apertures.

profiles. Since the magnetic field is very low in TPE-RX, we use the O-mode reflection, whose cutoff frequency is the plasma frequency, as

$$\frac{\omega_{cut}}{2\pi} = 28.4\sqrt{n_e[10^{19}\,\mathrm{m}^{-3}]}. \qquad (2)$$

With 20 GHz reflectometry, a cutoff density of $0.5\times10^{19}\,\mathrm{m}^{-3}$, density fluctuations can be observed when $n_{av} > 0.4\times10^{19}\,\mathrm{m}^{-3}$. In the typical TPE-RX plasma, the cutoff frequency near the field reversal surface, where

the toroidal field changes direction, is about 20 GHz. Therefore, we use 20 GHz for MIR in TPE-RX.

　Figure 2 shows a schematic diagram of the MIR system in TPE-RX. The quartz window of the TPE-RX viewing port is located at $r = 67$ cm, and the illumination wave (RF) can pass through the window. The primary mirror (M_1), an elliptic concave mirror with a size of 40 cm × 43 cm, generates a parallel illumination beam in the plasma. The reflected wave is collected by M_1 and is separated from the illumination beam using the first beam splitter (BS_1). The local oscillation (LO) wave and the reflected wave is mixed with the second beam splitter (BS_2). These beam splitters are 3-mm-thick Plexiglas plates. The RF wave reflected by BS_1 and the LO wave passing through BS_2 are absorbed by a microwave absorber to reduce background noise. An image of the reflection layer is projected on the 2-D mixer array using a the Teflon lens (L_1).

　The beam pattern of the microwaves is calculated by solving Maxwell's equations with the finite difference time domain method (FDTD) [6–8]. Figure 3 (a) shows the illumination microwave beam from the horn antenna of the RF source to the plasma. The diameter of the illumination beam is 9 cm at the window and 10 cm in plasma; therefore, the illumination beam is designed to pass through the window. The illumination wave is scattered by the plasma and accumulated by the main mirror. Figure 3 (b) shows the scattered wave at a single point in the plasma to the de-

tector. At the detector, the beam size is about 3 cm in this FDTD calculation. Figure 3 (c) shows the LO wave traveling to the detector. The beam size of the LO wave is about 5.5 cm at the detector.

In this experiment, two types of 2-D mixer arrays are used. One is a 2-D array of coax-to-waveguide adapters with diodes. The waveguide is for the frequency bandwidth of 18-26.5 GHz and has an inner size of 1.07 cm × 0.43 cm. These adapters are separated by 2.24 cm. Another is a 2-D planar Yagi-Uda antenna array on a Teflon printed circuit board (PCB) with a thickness of 0.254 mm. In this array, four elements are set on a PCB with a distance of 12 mm between them, and four PCBs are stacked with a distance of 15 mm between each pair. Each element consists of a planar Yagi-Uda antenna, a balun, a Schottky barrier diode (SBD) tip, and an IF amplifier. In this system, a tapered balun [9] is used, which is different from the original planar Yagi-Uda antenna system [10]. To design the antenna system, computer code for electro-magnetic fields was employed. This Yagi-Uda antenna has three guiding elements, a pair of dipole elements, and a reflector element. The IF amplifier consists of surface acoustic wave (SAW) bandpass filters and RF amplifiers. In addition, the mixer element has two voltage regulators for the amplifier's power supply and the SBD's DC bias. The signal output is a micro-miniature connector with a lock-snap mechanism (MMCX) straight PCB jack connector. The 2-D mixer array is contained in a shield box that has 16 sub-miniature version A (SMA) connectors for signal output. The MMCX and SMA are connected with a coaxial cable inside the shield box.

The LO wave ($\omega + \omega_1$) is created by mixing the RF wave (ω: 20 GHz) and the lower frequency wave generated by a crystal oscillator (ω_1: 110 MHz) at an up-converter. Lenses L_1 and L_2 focus the LO wave into a spot with a diameter of 10 cm on the 2-D mixer array. By mixing the reflected wave of frequency ω and the LO wave, the 2-D mixer array creates an IF signal of frequency ω_1. Since the IF frequency ω_1 is well stabilized, noise can be significantly reduced because the IF amplifier's bandwidth is narrow (4 MHz).

The reflected wave can be represented as, $A \exp[i(\omega t + \phi)]$, where the amplitude A and phase ϕ are generated by a density fluctuation in the plasma. The phase ϕ indicates vibration of the reflection layer. The IF signal can be represented as, $A \exp[i(\omega_1 t + \phi)]$. The amplitude is obtained by rectifying the IF signal with a microwave monolithic integrated circuit (MMIC). The phase is obtained by comparing the IF frequency and the signal using an IQ demodulator. The I and Q signals correspond to $\cos\phi$ and $\sin\phi$, respectively.

Because of RF noise, the rectified RF signal contains a large offset. This offset is removed by an offset canceler, which consists of a differential-amplifier and a sample-hold circuit. The sample-hold circuit works as follows: A digitizer samples the MIR data at $t = 0$ and stores it
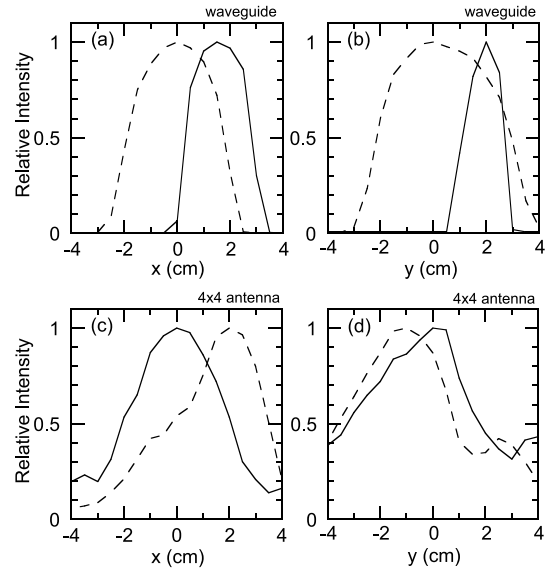

Fig. 4 Microwave profile detected using coax-to-waveguide adapters (a) in the poloidal direction and (b) in the toroidal direction. Microwave profile detected using the 2-D Yagi-Uda antenna array (c) in the poloidal direction and (d) in the toroidal direction. The solid and broken lines indicate neighboring detection channels.

in digital memory, and then a digital-to-analog converter generates analog output. This output represents the offset. The differential-amplifier subtracts the offset from the MIR signal.

As a test of the MIR system, reflected microwaves from a target are detected using this MIR system. The target is set 80 cm from the MIR enclosure, 133 cm from the primary mirror M_1, and 38 cm from the viewing port window. This position corresponds to a plasma minor radius of 30 cm. To simulate the viewing port, a sheet of microwave absorber with a 12-cm-diameter hole is set at the position of the viewing port window. The target is a rotating aluminum alloy disk with a 6.35-cm-diameter hole. This rotating disk is covered with a microwave absorber with a 4 cm × 4 cm square hole. When this hole is smaller than 3 cm × 3 cm, no signal is obtained. Figure 4 shows reflected signals when the target moves in the poloidal direction (x) and the toroidal direction (y). Signals shown in Figs. 4 (a)-(b) are detected using the K-band coax-to-waveguide adapter array. Signals shown in Figs. 4 (c)-(d) are detected using the 2-D Yagi-Uda antenna array. For the coax-to-waveguide adapter array, the spatial resolution at the plasma is between 3 and 5 cm, and the channel separation is between 1.5 and 2 cm. In the case of the Yagi-Uda antenna array, the spatial resolution at the plasma is between 2.5 and 5 cm, and the channel separation is between 1 and 3 cm.

3. Experimental Results in TPE-RX

TPE-RX has the following operation modes [3]: standard RFP plasma, high-Θ plasma, PPCD plasma [13, 14], and quasi-single helicity (QSH) plasma [15]. Here, F and Θ are the toroidal and poloidal fields, respectively, normalized by the average toroidal field at the plasma boundary, and are defined as

$$\Theta = \frac{B_{\mathrm{p}}(a)}{\langle B_{\mathrm{t}} \rangle}, \quad F = \frac{B_{\mathrm{t}}(a)}{\langle B_{\mathrm{t}} \rangle}. \tag{3}$$

Subscripts p and t denote the poloidal and toroidal directions, respectively. Those plasmas differ in the following characteristics: The high-Θ plasma has a high poloidal field, and it is sometimes accompanied by a sawtooth oscillation, which is a typical dynamo phenomenon. In PPCD operation, the poloidal current in the edge plasma is inductively driven in order to suppress the dynamo effect. Thus, it is expected that instabilities in the PPCD plasma are reduced, and the PPCD plasma is expected to exhibit higher confinement than the other operation modes. In sum, the high-Θ plasma is the opposite of the PPCD plasma. In the QSH plasma, a single helical structure stays inside the RFP plasma. This paper presents MIR data on the standard RFP, high-Θ, PPCD, and QSH plasmas.

3.1 Standard and high-Θ plasmas

Figures 5 (a)-(e) show the plasma current (I_{p}), line-averaged electron density (n_{e}), F, Θ, soft X-ray signal (SX), cut-off radius of 20 GHz (r_{cut}) and MIR signal in the case of a high-Θ RFP plasma in TPE-RX. The cut-off surface of 20 GHz is normalized by the minor radius ($a = 45$ cm). The MIR signal represents density fluctuations near $r/a = 0.8$, which is near the field reversal surface. After $t = 0.03$ s, the cutoff surface seems to disappear, but the amplitude of MIR fluctuation is still high. This may be due to errors in density estimation, which are caused by mistaken assumptions about the density profile (a more peaked profile may be possible) and/or an error in the measurement itself, such as insufficient compensation for mechanical vibration.

In this case, the 2-D Yagi-Uda antenna array is employed. Figure 5 (f) shows MIR channel numbers at the detector position schematically. Here, subscripts p and t denote the poloidal and toroidal directions, respectively. Since the imaging optics make vertical inverted images, the p direction corresponds to the positive sign in the plasma, and the t direction corresponds to the clockwise direction in the top view. As waveforms are similar to those in other channels, the 2-D receiver works well. Examples of MIR signals from this plasma are shown in Figs. 6 (a)-(b). Figure 6 (a) shows fluctuations in the standard RFP plasma with $\Theta = 1.5$ at $t = 0.019$ s. Figure 6 (b) shows fluctuations in the high-Θ plasma with $\Theta = 1.7$ at $t = 0.029$ s. In both cases, the MIR signal contains many short-period bursts of waves with different frequencies. The signal contains high-frequency components in the case of the high-Θ
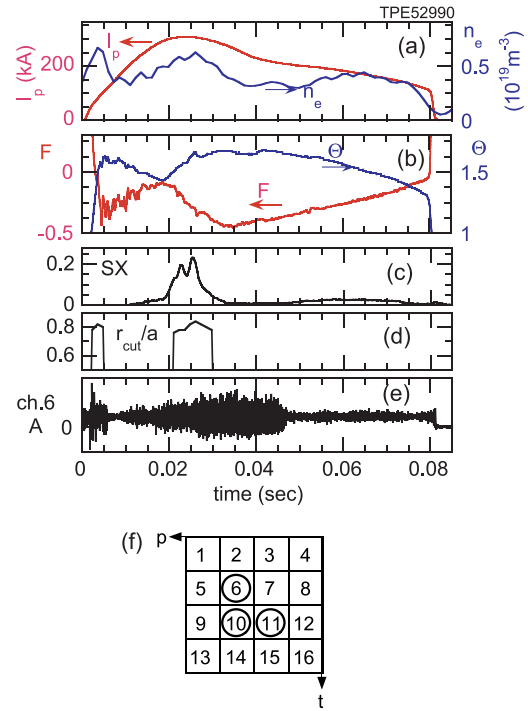
Fig. 5 Plasma parameters in high-Θ operation in TPE-RX. (a) The plasma current (I_{p}) and line-averaged density (n_{e}); (b) F and Θ; (c) soft X-ray signal; (d) radius of reflection layer of MIR microwaves (cutoff radius); (e) signal of MIR ch.6. (f) schematic view of the 2-D mixer array.
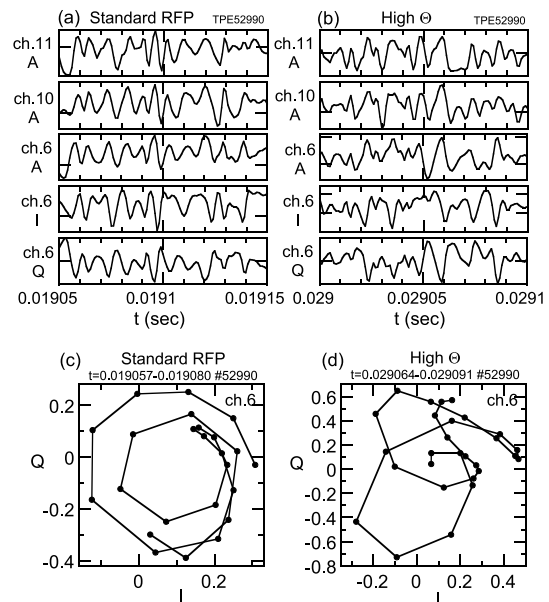
Fig. 6 MIR signal in high-Θ operation in TPE-RX. (a) MIR signals during the period of the standard RFP plasma. (b) MIR signals during the period of the high-Θ RFP plasma. (c) Lissajous' curve of I-Q signals from ch.6 in standard RFP plasma ($t = 0.019057 - 0.019080$ s). (d) Lissajous' curve of I-Q signals from ch.6 in high-Θ RFP plasma ($t = 0.029064 - 0.029091$ s).
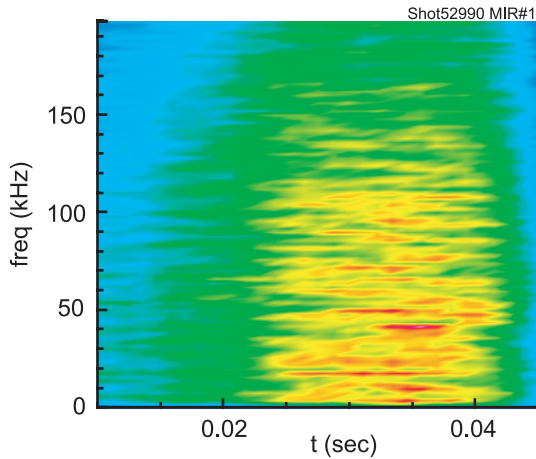
Fig. 7 Power spectra of the MIR signal in the high-Θ plasma.

plasma.

Figures 6 (c)-(d) show the Lissajous' curve of I-Q signals from ch. 6. If the I and Q signals are proportional to $\cos\phi$ and $\sin\phi$, respectively, the Lissajous' curve should be a circle. The operation of the I-Q detector is confirmed on the test bench as follows: The Lissajous' curve is circular, and the trajectory rotates as the phase ϕ is changed. In the experiment, however, the Lissajous' curve is not a circle, and the center of the closed curve is shifted from the origin. This phenomenon is predicted by a reflectometry theory [11]. The trajectory indicates how the reflection layer moves. Closed circles indicate data points, which are taken every 1 μs. In Fig. 6 (c), at the point (I, Q)=(0.14, 0.1), which corresponds to t = 0.019069 s, the direction of the trajectory reversed. This indicates that the reflection layer first moves in one direction and then reversed at t = 0.019069 s. A similar phenomenon is also observed in the high-Θ plasma. As shown in Fig. 6 (d) the trajectory reverses direction at (I, Q)=(0.47, 0.08), which corresponds to t = 0.02908 s.

Figure 6 shows differences between the standard RFP and the high-Θ plasmas. In the case of the high-Θ plasma, MIR signals contain many oscillations with different frequencies. This feature appears in the Fourier spectrum. Figure 7 shows the Fourier spectra of the MIR signal from ch. 6 in the shot described in Fig. 6. In the case of high-Θ RFP plasma, the spectrum spreads from 5 to 150 kHz. Comparing Fig. 6 (c) and (d), we can see how the Lissajous' curves in the standard RFP and in the high-Θ plasmas differ. Lissajous' curves of the standard RFP plasma appears as concentric circles, possibly indicating that the reflection layer vibrates. Lissajous' curves of the high-Θ plasma are not concentric circles, and the area of the trajectory is much bigger than that of the standard RFP plasma. This may indicate that the motion of the reflection layer in the high-Θ RFP plasma is greater and more complicated than that in the standard RFP.
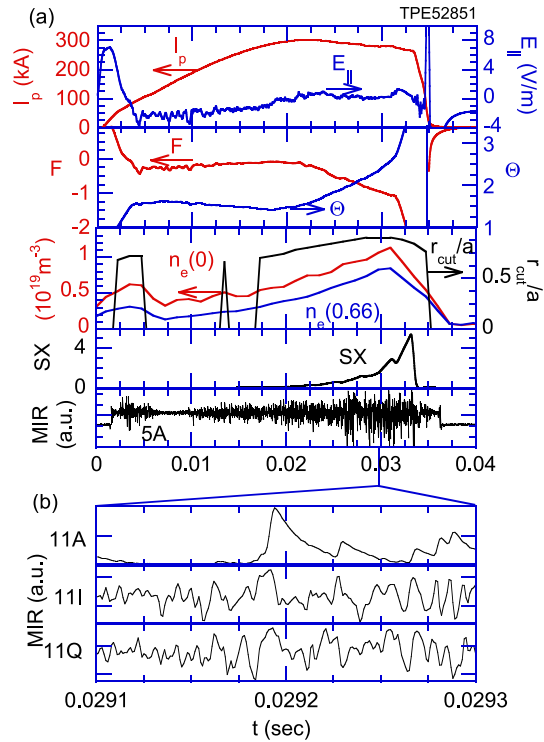

Fig. 8 (a) The plasma current (I_p), toroidal electric field ($E_{\parallel}$), F, Θ, line-averaged electron density (n_e), cut-off radius (r_{cut}) of 20 GHz, soft X-ray signal (SX), and MIR signal in the case of PPCD operation in TPE-RX. (b) Amplitude, I, and Q of the central channel (ch. 11) of the 4×4 Yagi-Uda antenna array.

3.2 PPCD plasma

Figure 8 (a) shows plasma current, the toroidal electric field ($E_{\parallel}$), F, Θ, line-averaged electron density, cut-off radius of 20 GHz, soft X-ray signal, and MIR signal in the case of PPCD operation in TPE-RX. The PPCD power supply is turned on at t = 0.02 s, after which Θ increases and F decreases. During PPCD, the soft X-ray signals increase until plasma termination. The soft X-ray signal is more than 20 times stronger than that of the high-Θ plasma shown in Fig. 5. Thus, the PPCD plasma has higher confinement than the typical RFP plasma. Figure 8 (b) shows the amplitude, I, and Q of the central channel (ch. 11) of the 4×4 Yagi-Uda antenna array. Channel numbers are defined as shown in Fig. 5 (f). The MIR signal contains many short period bursts of waves with different frequencies.

To present the position of fluctuations, Fig. 9 shows the root means square (RMS) of the total MIR fluctuation before and during PPCD. Twelve shots with similar plasma parameters are accumulated in this figure. Fluctuations before PPCD are smaller than during PPCD. During PPCD, the fluctuation is enhanced near r/a = 0.88, or r = 40 cm. In other regions, the fluctuation level during PPCD is similar to that before PPCD.

Figure 10 shows an example of the power spectrum of MIR signals in the PPCD plasma. The Fourier analysis
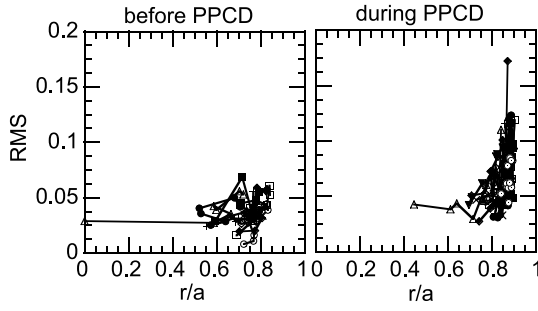
Fig. 9 Root means square (RMS) of the total MIR fluctuation (a) before PPCD and (b) during PPCD. Twelve shots with similar plasma parameters are accumulated. Different marks indicate different shots, and lines connecting marks indicate trajectories over 10 ms.
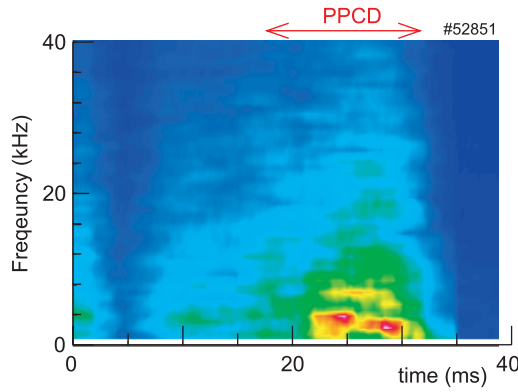

Fig. 10 Power spectra of MIR signals in the PPCD plasma.

Fig. 11 plasma current, quasi-single helicity (QSH) indicator (NS), F, Θ, minor radius of the MIR reflection layer (cut-off radius), and signal of MIR ch.1 in the QSH plasma.

Fig. 12 Power spectra of MIR signals in the QSH plasma.

technique used here is presented elsewhere [12]. During PPCD operation, a magnetohydrodynamic (MHD) mode with a frequency of 3 kHz predominates. This MHD mode may be enhanced because of the high plasma pressure gradient in the edge region.

3.3 QSH plasma

Figure 11 shows the plasma current, QSH indicator (NS), F, Θ, cut-off radius of 20 GHz, and MIR signal of a QSH plasma in TPE-RX. In this case, microwaves are detected using a 2×2 array of K-band coax-to-waveguide adapters with diodes. Here, NS is defined as

$$NS = 1/ \sum_{j=n_1}^{n_2} \left[\frac{\delta B_{mj}^2}{\sum_{k=n_1}^{n_2} \delta B_{mk}^2} \right]^2. \qquad (4)$$

The state $NS = 1$ indicates that the plasma is governed by a single helical mode. In Fig. 11, we take $m = 0$, $n_1 = 1$ and $n_2 = 10$. The QSH mode starts at $t = 0.05$ s. The cut-off radius of 20 GHz is nearly $r/a = 0.5$, which is at the middle of the plasma. Figure 12 shows an example of the power spectrum of MIR signals in the QSH plasma. Before QSH mode (standard RFP), the spectrum is broad. During QSH mode, a single spectrum with a frequency of
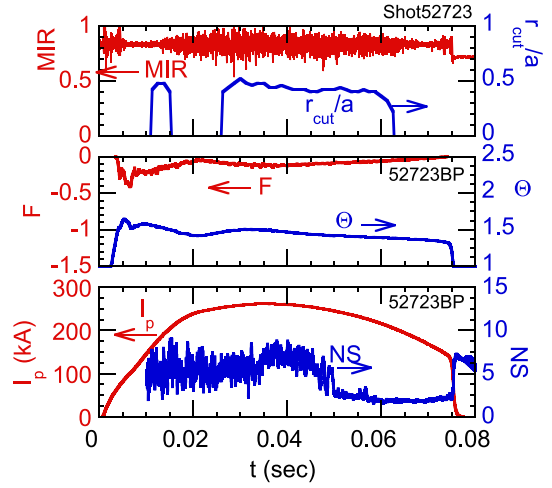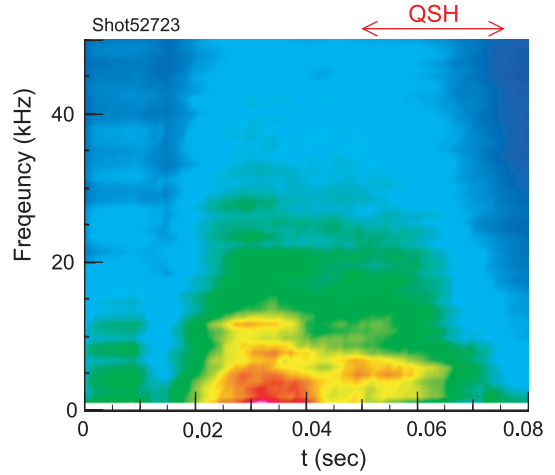
5 kHz predominates.

4. Summary and Discussion

The second generation MIR has been installed in TPE-RX. In this system, the IF frequency, which is the difference between the reflected wave and the LO wave, is stabilized so that sensitive measurement is possible. This is one reason that the 2-D imaging detector array with a planar Yagi-Uda antenna works well. This paper presents preliminary experimental results of the standard RFP, high-Θ, PPCD, and QSH plasmas. The density fluctuation signal contains many short-period bursts of waves with different frequencies in RFP plasma. This is quite different from a tokamak plasma, where usually a single MHD mode persists. The FFT power spectra of these four plasmas examined differ as follows: In the case of the high-Θ RFP plasma, the frequency spectrum is very widel (from 5 to

150 kHz). The PPCD plasma has a strong MHD mode that is localized at the plasma edge, and the frequency is much lower than for the standard RFP plasma. In the QSH plasma, the amplitude of the MIR fluctuation is smaller and the Fourier spectrum width is narrower than those of the standard RFP plasma. The MIR fluctuation is strongest in the PPCD plasma, but the soft X-ray signal that indicates the plasma performance is 10 times stronger than that for the other plasmas. This MHD mode may be caused by the plasma pressure due to good plasma confinement. The high-Θ plasma may have poor confinement, because the soft X-rays disappeared and the electron density decreased. In this case, the frequency spectrum extends to a high-frequency region. Therefore, confinement may be related to the mode structure. This result is very encouraging for the development of MIR.

[1] E. Mazzucato, Rev. Sci. Instrum. **69**, 2201 (1998).
[2] H. Park *et al.*, Rev. Sci. Instrum. **74**, 4239 (2003).
[3] Y. Yagi *et al.*, Nucl. Fusion **45**, 138 (2005).
[4] S. Yamaguchi *et al.*, Rev. Sci. Instrum. **77**, 10E930 (2006).
[5] S. Yamaguchi *et al.*, Plasma Fusion Res. **2**, S1038 (2007).
[6] H. Hojo, Y. Kurosawa and A. Mase, Rev. Sci. Instrum. **70**, 983 (1999).
[7] H. Hojo, T. Uruta, A. Fukuchi and A. Mase, Rev. Sci. Instrum. **73**, 387 (2002).
[8] M. Ignatenko, A. Mase, L. G. Bruskin, Y. Kogi and H. Hojo, Rev. Sci. Instrum. **75**, 3810 (2004).
[9] W. Duncan and V.P. Minerva, Proc. IRE **48**, 156 (1960).
[10] W.R. Deal *et al.*, IEEE Trans. Microwave Theory Tech. **48**, 910 (2000).
[11] A. Ejiri, T. Yamada, Y. Adachi, O. Watanabe and Y. Takase, Phys. Control. Fusion **50**, 065003 (2008).
[12] Z.B. Shi, Y. Nagayama, S. Yamaguchi, Y. Hamada and Y. Hirano, Plasma Fusion Res. **3**, S1045 (2008).
[13] Y. Yagi *et al.*, Plasma Phys. Control. Fusion **44**, 335 (2002).
[14] L. Frassinetti *et al.*, Plasma Phys. Control. Fusion **49**, 199 (2007).
[15] Y. Hirano, H. Koguchi, K. Yambe, H. Sakakita and S. Kiyama, Phys. Plasmas **13**, 122511 (2006).